International Journal of Applied Earth Observation and Geoinformation 143 (2025) 104826

Contents lists available at ScienceDirect

International Journal of Applied Earth Observation and Geoinformation

journal homepage: www.elsevier.com/locate/jag

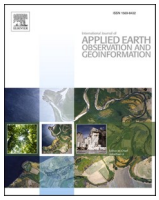

Water transparency and color in large rivers observed by Sentinel-2 MSI and its implications for SDG 6.3.2 monitoring

Xuezhu Jiang [a,b,c], Shenglei Wang [a,b,*], Junsheng Li [a,b,d], Evangelos Spyrakos [e], Huaxin Yao [a,b,c], Fangfang Zhang [a,b], Andrew N. Tyler [e], Bing Zhang [a,c]

[a] Key Laboratory of Digital Earth Science, Aerospace Information Research Institute, Chinese Academy of Sciences, Beijing 100094, China
[b] International Research Center of Big Data for Sustainable Development Goals, Beijing 100094, China
[c] College of Resources and Environment, University of Chinese Academy of Sciences, Beijing 100049, China
[d] School of Electronic, Electrical and Communication Engineering, University of Chinese Academy of Sciences, Beijing 100049, China
[e] Earth and Planetary Observation Sciences (EPOS), Department of Biological and Environmental Studies, Faculty of Environmental Sciences, University of Stirling, Stirling, United Kingdom

ARTICLE INFO

Keywords:
Secchi disk depth
Forel-Ule Index
Water quality
Sentinel-2
Rivers

ABSTRACT

Rivers are vital to Earth's water cycle and human societies, yet their water quality is increasingly threatened by climate change and human activities. While satellite remote sensing has emerged as a powerful tool for large-scale water quality monitoring across diverse aquatic ecosystems, a systematic analysis of water optical properties in rivers remains limited, restricting its use in supporting Sustainable Development Goal (SDG) monitoring. This study presents the first comprehensive analysis of water transparency (Secchi disk depth, Z_{SD}) and color (Forel-Ule Index) in the five large rivers (Yangtze, Danube, Mississippi, Nile, and Amazon) using Sentinel-2 MSI data (2019–2021). Results reveal significant spatial-seasonal variations: Danube had the highest transparency (Z_{SD}) and bluest color (FUI), followed by Nile, Yangtze, Mississippi, and Amazon. These differences were primarily driven by basin-specific soil erodibility and precipitation. Spatially, the Yangtze, Mississippi, and Amazon exhibited decreasing Z_{SD} and increasing FUI from their upper to lower reaches, contrasting with different trends in Danube and Nile, highlighting the influence of large dams. Seasonally, two different patterns were observed in the five rivers, underscoring the hydrological influences on water optical properties. Furthermore, as two key optical water quality parameters, Z_{SD} and FUI were analyzed for their complementary roles in characterizing river turbidity across varying water conditions. By quantifying spatiotemporal patterns, this study establishes a global baseline for river optical properties and supports SDG 6.3.2 monitoring. Our findings offer new insights into large-scale river ecosystem dynamics under environmental change.

1. Introduction

Rivers serve as vital components of the global water cycle, linking lakes, reservoirs, oceans, and land while sustaining ecosystems and water resources (Vörösmarty et al., 2010). As a primary freshwater source, they support human health, ecological balance, and economic activities (Huang et al., 2021). However, climate change, increased human activities, and population growth in recent decades have significantly impacted the sustainability of global river systems (Ceola et al., 2019). Over 10 % of the global population resides in the basins of Yangtze, Danube, Mississippi, Nile, and Amazon rivers (Doxsey-Whitfield et al., 2015). These rivers have played central roles in the socioeconomic development of the continents. As such water quality of the large rivers has been a major concern of the local societies.

Monitoring these complex river systems remains challenging, as they are dynamic systems that change over temporal and spatial scales (Van Vliet et al., 2023). Traditional ways of monitoring water quality using ground samples often struggle to capture these changes. Remote sensing methods offer a more effective alternative, as they enable continuous, extensive, and cost-effective monitoring of water quality, although the uncertainty incorporated with the retrieved water quality parameters caused by the complexity of water body optical properties cannot be ignored (Kuhn et al., 2019; Luo et al., 2025; Sun et al., 2025; Werther et al., 2022; Yue et al., 2024). Considering the narrow, elongated, and

* Corresponding author.
E-mail address: wangsl@radi.ac.cn (S. Wang).

https://doi.org/10.1016/j.jag.2025.104826
Received 5 May 2025; Received in revised form 19 August 2025; Accepted 28 August 2025
Available online 7 September 2025

dynamic characteristics of rivers, higher demands are placed on the spatial resolution, temporal resolution, and spectral resolution of satellite remote sensing. This also brings more challenges to the remote sensing monitoring of river water quality (Qiu et al., 2024; Wu et al., 2023; Zhang et al., 2023b). The new generation of satellites, exemplified by the Sentinel-2 Multispectral Instrument (MSI), with their high spatial resolution, diverse spectral bands, and frequent revisit, offers significant opportunities for river water quality monitoring (Wang et al., 2024).

Water transparency and water color have a long history and are intuitive parameters used to assess water quality (Wang et al., 2019). Their tight coupling with both physical and biogeochemical processes of water bodies across multiple spatial and temporal scales maintains their critical role in modern aquatic environment monitoring (Brewin et al., 2023). Water transparency, indicating water clarity, can be measured by lowering a Secchi disk into the water until it is no longer visible. The vertical distance from water surface to the point where the disk disappears is called Secchi disk depth (Z_{SD}) (Lee et al., 2018a) (Fig. 1a,b). Water color, evaluated by the Forel-Ule Index (FUI), is determined by the three main water quality constituents: chlorophyll-a (Chla), total suspended matter (TSM), and colored dissolved organic matter (CDOM) (Wang et al., 2021). The FUI classifies color of the ocean and inland waters worldwide into 21 levels, ranging from deep blue to reddish-brown (Van der Woerd and Wernand, 2015) (Fig. 1c,d). Due to their low cost and ease of acquisition, both water transparency and color have been extensively utilized for measurements in both global inland and ocean waters, and have been widely employed to monitor changes in water turbidity (Lee et al., 2018b; Ye and Sun, 2022). This has facilitated the expansion of their applications through numerous scientific projects and studies (Maciel et al., 2023; Wang et al., 2021).

As two water optical variables, Z_{SD} and FUI can be effectively retrieved via optical satellite data (Lee et al., 2015; Van der Woerd and Wernand, 2015). Due to the ease of obtaining in situ measurements for the two parameters, their retrieval have undergone extensive validation and refined over time to constrain the uncertainties and improve the adaptability across various water types and conditions (Jiang et al., 2019; Liu et al., 2019; Van der Woerd and Wernand, 2018). This facilitates Z_{SD} and FUI to play key roles in understanding the changes in water ecosystems in global and regional lakes and oceans, effectively compensating for the limitations of other bio-physical water quality parameters in terms of model applicability and uncertainty (Duan et al., 2025; He et al., 2022; Maciel et al., 2023; Song et al., 2022; Wen et al., 2024). However, due to the unique nature of rivers, except few studies on regional scales (Fabricius et al., 2016; Gardner et al., 2021), research on using satellites to monitor the optical properties of rivers across the globe remains limited, which hinders our ability to fully understand changes in river ecology and water quality around the world (Li et al., 2024). Moreover, comparative studies focusing on the optical variables of river water are particularly scarce, which may limit the ability to evaluate their respective sensitivities and complementarities under diverse riverine conditions.

This study used Sentinel-2 MSI data to analyze the Z_{SD} and FUI changes in five of the most representative large rivers across five continents—the Yangtze, Danube, Mississippi, Nile, and Amazon from 2019 to 2021. The existing algorithms for Z_{SD} and FUI were first tested and validated in the rivers. This study represents the first map of the spatial and seasonal variations in the optical properties of these five large rivers

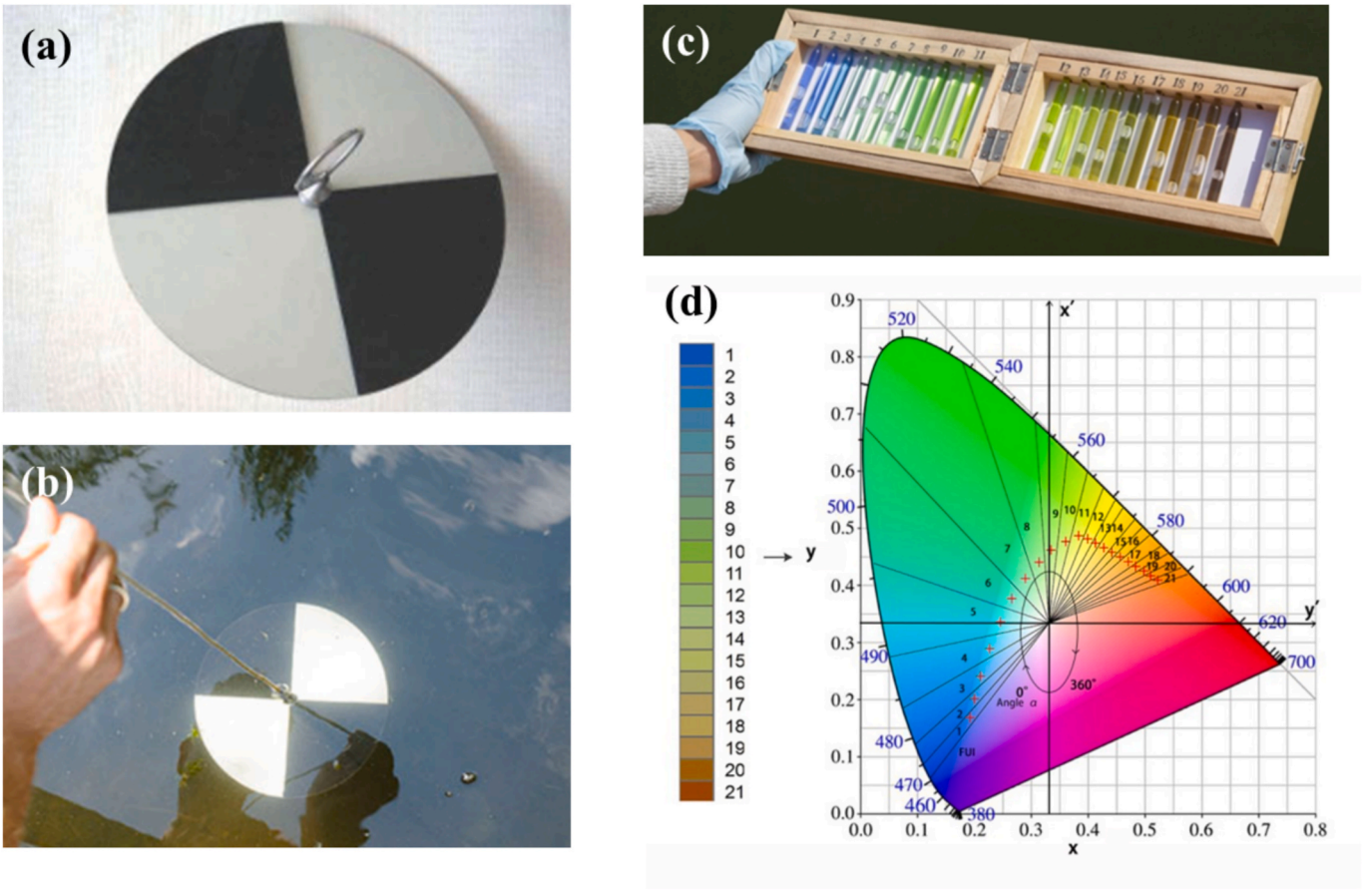

Fig. 1. (a) The Secchi disk; (b) Water transparency measurement in the field work, where it is determined as the vertical distance from water surface to the point where the Secchi disk is no longer visible; (c) The Forel-Ule Scale; (d) Chromaticity coordinates and division diagram of Forel-Ule Index (FUI) in the International Commission on illumination (CIE) chromaticity diagram (
adapted from Wang et al. (2018)).

and provides a comparative assessment of these two key optical variables. Additionally, it examines the environmental factors associated with these variations, aiming to elucidate the water quality characteristics of rivers across different global regions and their potential environmental implications.

2. Data and methods

2.1. Study area

In this study, we chose one of the largest exorheic rivers from each of the five continents (excluding Oceania and Antarctica) to ensure the rivers represented global regions. The selected rivers include the Yangtze in Asia, the Danube in Europe, the Mississippi in North America, the Nile in Africa, and the Amazon in South America (Fig. 2). These rivers contribute around 27 % of the total estimated global river water discharge into the sea (Peucker-Ehrenbrink, 2009), and they span a broad range of climatic zones, land use patterns, and hydrological regimes, making them suitable for global comparative analysis.

The Yangtze, the largest in Asia, is characterized by high sediment fluxes driven by intensive agricultural and industrial activities in its basin (Yang et al., 2004). The hydrology of the Yangtze is strongly dominated by the subtropical monsoon climate, resulting in peak flows during the summer season. Large dams, particularly the Three Gorges Dam, significantly modify downstream turbidity and flow regimes (Zhang et al., 2016).

The Danube flows through multiple European countries and lies between temperate oceanic, temperate continental, and Mediterranean climate zones. Historically, the river suffered from significant pollution due to industrial and agricultural activities (Gasparotti, 2014). It has been managed under international cooperation frameworks since the implementation of the Danube River Protection Convention in 2000 (Sommerwerk et al., 2010).

The Mississippi is a sediment-rich system heavily influenced by agricultural runoff and extensive river engineering (Yin et al., 2023). The river's hydrological regime is primarily governed by continental

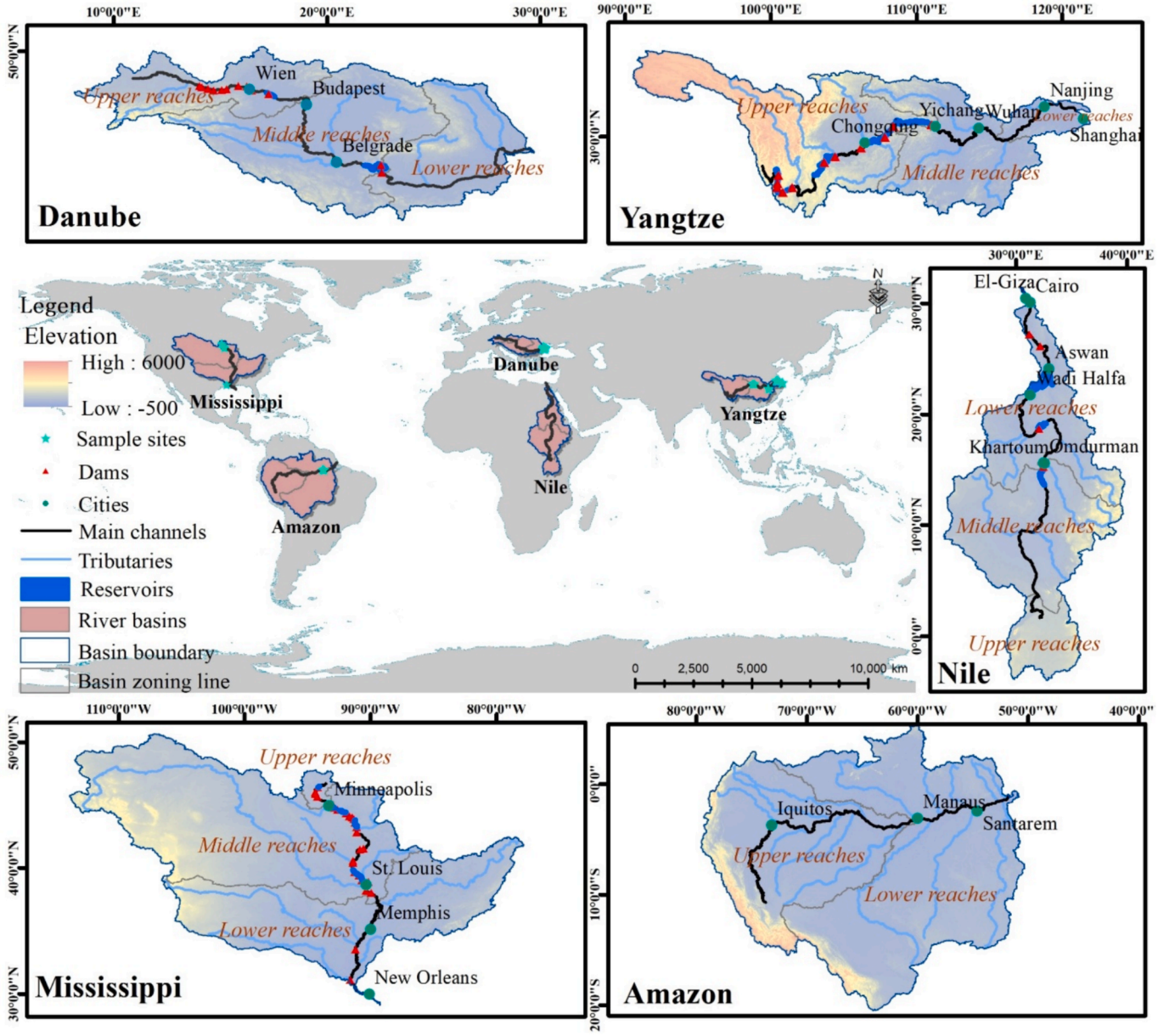

Fig. 2. Spatial distribution of the five studied river basins, showing major dams and reservoirs (GeoDAR; Wang et al. (2022)), river networks (GRNWRZ; Yan et al. (2019)), cities, and sampling sites. River segments are classified into upper, middle, and lower reaches based on HydroBASINS (Lehner and Grill, 2013).

climatic patterns, characterized by snowmelt in the upper reaches and seasonal precipitation (Yeşilköy et al., 2024).

The Nile is affected by tropical savanna and desert climates, with minimal rainfall contribution except from the Ethiopian Highlands during the wet season (Camberlin, 2009). Its water quality is reported to be influenced by strong seasonal contrasts, reservoir regulation (e.g., Aswan High Dam), and intensive irrigation (Elshemy and Meon, 2017).

The Amazon is the world's largest river by discharge. Its tropical rainforest climate results in year-round high temperatures and abundant rainfall (Liang et al., 2020). Although the basin remains largely forested, significant deforestation in certain regions has led to increased sediment and nutrient loads, causing disturbances to the riverine environment (Narayanan et al., 2024).

2.2. Dataset

2.2.1. Sentinel-2 MSI data and preprocessing

The Sentinel-2 program consists of two polar-orbiting satellites, Sentinel-2A and Sentinel-2B, both of which are equipped with the MSI (Drusch et al., 2012). In this study, Sentinel-2 Level-2A (L2A) surface reflectance (SR) images were obtained from Google Earth Engine (GEE) (Main-Knorn et al., 2017), and only images with less than 40 % cloud cover were selected. Sentinel-2 L2A products are atmospherically corrected using the Sentinel-2 Atmospheric Correction Processor (Sen2Cor) (Louis et al., 2016), which performs terrain and atmospheric correction to generate SR images. The performance of Sentinel-2 L2A products over water bodies has been demonstrated to be effective in previous studies (Ali et al., 2024; Toming et al., 2016). To further remove the pixels affected by clouds, the QA60 band with cloud mask information was used for masking out the opaque cloud, cirrus cloud, and cloud shadow pixels flagged in the QA60 band (Corbane et al., 2020). A simple satellite SR product correction method was applied, which calculates water reflectance by subtracting the minimum value of the SWIR band from the visible and NIR bands and then dividing by π (Wang et al., 2016). The results of this method were found to be satisfactory for a wide range of inland water bodies (Cao et al., 2022).

River boundaries frequently shift due to fluctuations in river channels and water volumes (Chadwick et al., 2022); therefore, we used only the river centerlines for analysis, as illustrated in the processing workflow in Fig. 3. In this study, the main river channels were identified based on annual water history datasets provided by the European Commission's Joint Research Centre (JRC), and a 1 km buffer zone was established (Pekel et al., 2016). The Modified Normalized Difference Water Index (MNDWI) was calculated within this buffer, and the Otsu method, an automatic thresholding technique that minimizes intra-class variance and maximizes inter-class variance, was subsequently employed to determine the optimal threshold for water bodies, producing the river mask (Otsu, 1979). To avoid the effect of land adjacency, the RivWidthCloud automatic extraction algorithm was utilized on the river mask to generate a clean river centerline (Yang et al., 2020). Given that the highest spatial resolution of Sentinel-2 MSI is 10 m, we selected the centerline of river sections with a width exceeding 50 m as our study areas. This selection helps mitigate the impact of mixed pixels, land-adjacent pixels, and shallow optical water. The lengths of the selected river sections are as follows: Yangtze 4791 km, Danube 3630 km, Mississippi 4026 km, Nile 5866 km, and Amazon 5163 km. Subsequently, analyses were conducted using only Z_{SD} and FUI values computed along these river centerlines.

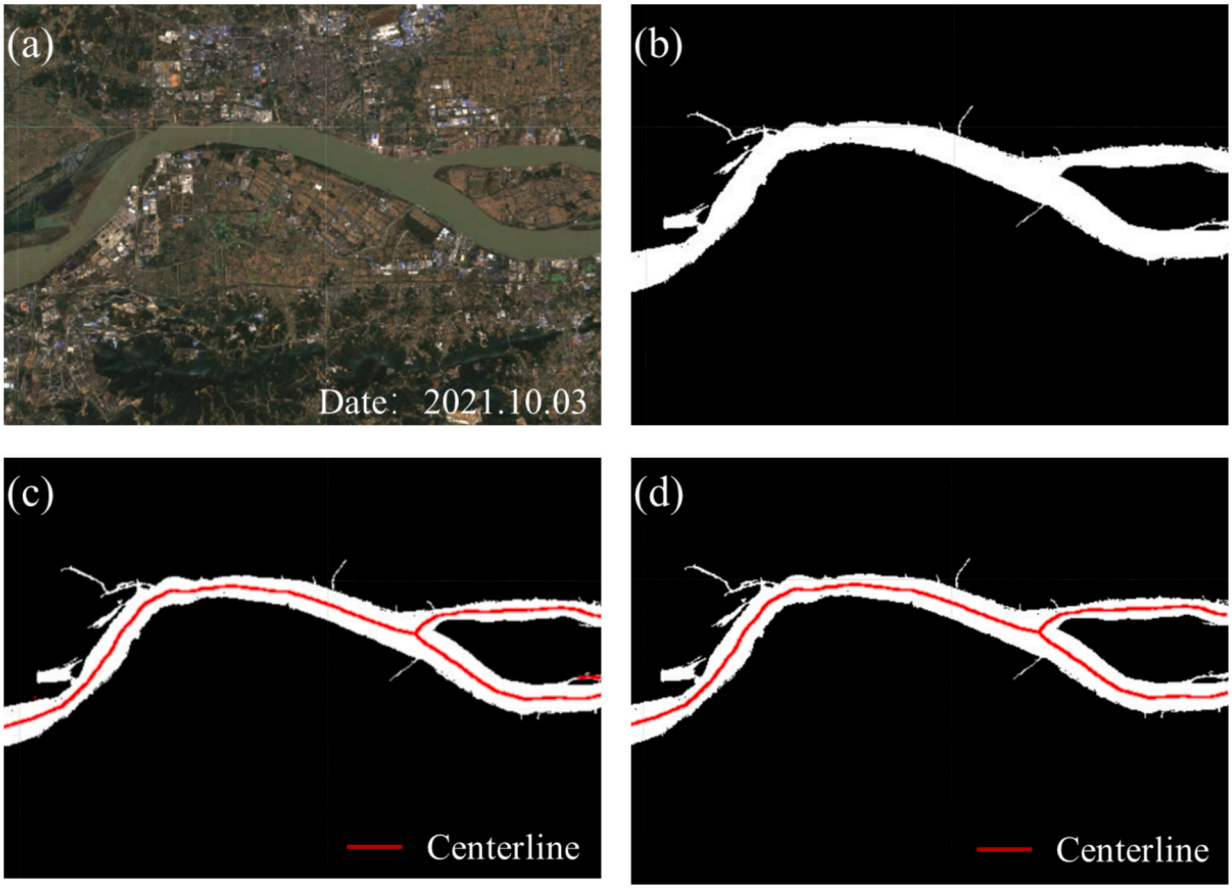

Fig. 3. Steps to derive the river centerlines. (a) Sentinel-2 MSI RGB image. (b) River mask. (c) 1-pixel-wide centerline. (d) Final centerline after removing sections narrower than 50 m.

2.2.2. In-situ data

Validation data were sourced from the GLORIA dataset (Lehmann et al., 2023) and acquired from Wang et al. (2024). The Z_{SD} and remote-sensing reflectance (R_{rs}) data used in this study were collected from the main channels, estuaries, and river-connected lakes and reservoirs of Yangtze, Danube, Mississippi, and Amazon, with all locations marked in Fig. 2. Z_{SD} was determined with a black-and-white Secchi disk, tied to a rope and lowered into the water until it vanished from view, marking the Z_{SD} depth. R_{rs} data were recorded using radiometers such as the TriOS-RAMSES, ASD FieldSpec, and Satlantic HyperGun, with R_{rs} spectra interpolated from the original sensor bandwidths to a 1 nm resolution. FUI was determined with the *in-situ* R_{rs} data following the method described in Wang et al. (2024).

2.2.3. Environmental auxiliary data

This study collected a set of environmental variables—including climatic, hydrological, anthropogenic, watershed, and land cover factors—to analyze their influence on river water quality. The climate data included precipitation (PRE), wind speed (WS), and temperature (TEMP). Hydrological data consisted of water level (WL) measurements. Human activity indicators encompassed dam and lake locations, population density, and gross domestic product (GDP). Watershed characteristics incorporated catchment area (CA) and soil erodibility factor (K). Land cover data focused on vegetation coverage rate (VCR). Detailed data sources and processing methods are provided in Text S1 and Table S1.

2.3. Z_{SD} and FUI inversion method

The study employed two key approaches for water quality assessment: the Quasi-Analytical Algorithm (QAA) for Z_{SD} retrieval and the FUI for water color classification. Z_{SD} inversion was performed using QAA_v6, a semi-analytical model that estimates transparency based on radiative transfer theory, particularly suitable for turbid inland waters (Lee et al., 2015). The algorithm derives absorption (a) and backscattering (b_b) coefficients from remote-sensing reflectance (R_{rs}), ultimately computing Z_{SD} from the diffuse attenuation coefficient (K_d). FUI inversion was derived from Sentinel-2 MSI data by calculating CIE tristimulus values (X, Y, Z), chromaticity coordinates (x, y), and hue angle (α), followed by a delta (Δ) correction to account for sensor-induced color distortions. The final FUI was determined using a hue angle lookup table (Wang et al., 2024). Detailed mathematical formulations and processing steps are provided in Text S1 and S3.

2.4. Spatial and seasonal analysis

Considering that the seasonal distribution patterns of Z_{SD} and FUI may be influenced by climatic factors such as temperature, precipitation, and water level (Pitarch et al., 2021; Zhang et al., 2023a), Z_{SD} and FUI measurements were taken along the centerlines of the rivers over three years, and seasonal averages for spring, summer, autumn, and winter were calculated. These seasonal averages were then used to determine the overall distribution of Z_{SD} and FUI across different areas. The Yangtze, Danube, Nile, and Mississippi, primarily located in the Northern Hemisphere, have seasons as follows: spring from March to May, summer from June to August, autumn from September to November, and winter from December to February. The Amazon, mainly in the Southern Hemisphere, experiences its spring from September to November, summer from December to February, autumn from March to May, and winter from June to August. To simplify the display and analysis, average Z_{SD} and FUI were computed every 20 km along the main channels of these five rivers.

The accuracy of Z_{SD} and FUI algorithms was evaluated using the coefficient of determination (R^2), mean absolute error (MAE), mean relative error (MRE), and bias. R^2 evaluates how well the model explains the variance in the observed data; MAE quantifies the average magnitude of absolute prediction errors; MRE represents the average relative difference between observed and estimated values as a percentage; and bias describes the systematic direction of the error, indicating systematic over- or under-prediction (Seegers et al., 2018). The formulas for each metric are provided in Equations (1)–(3).

$$R^2 = 1 - \frac{\sum_{i=1}^{N}\left(X_{m(i)} - X_{o(i)}\right)^2}{\sum_{i=1}^{N}\left(X_{o(i)} - \overline{X_o}\right)^2}\# \tag{1}$$

$$MAE = \frac{1}{N} \times \sum_{i=1}^{N} \left|X_{m(i)} - X_{o(i)}\right|\# \tag{2}$$

$$MRE = \frac{1}{N} \times \sum_{i=1}^{N} \frac{\left|X_{m(i)} - X_{o(i)}\right|}{X_{o(i)}} \times 100\%\# \tag{3}$$

$$Bias = \frac{1}{N} \times \sum_{i=1}^{N} \left(X_{m(i)} - X_{o(i)}\right)\# \tag{4}$$

In the equation, X_o represents the *in-situ* observed parameters, X_m represents the model-estimated parameters, and N is the number of samples.

Various statistical methods were employed to evaluate the trends and significant differences in Z_{SD} and FUI across different seasons and river segments. First, the Shapiro-Wilk test was used to assess whether the data followed a normal distribution (González-Estrada et al., 2022). Since the data did not distribute normally ($p < 0.05$), the Mann-Whitney U test was applied to determine differences between seasons and river segments. The Mann-Kendall test helped identify whether there were any trends in Z_{SD} and FUI from the river's source to its mouth during different seasons (Mann, 1945). Additionally, a moving window with a size of 3 was employed to identify sharp change points in Z_{SD} and FUI along the river from the upper to lower reaches. For each window, the mean and standard deviation were calculated, and a segment was identified as a sharp change point if the difference in means between consecutive windows exceeded three times the standard deviation of the previous window. For each identified sharp change point, we further examined whether there were dams, reservoirs, or tributary entries within 20 km of the location.

Pearson correlation analysis was performed to quantify the relationships between seasonal mean optical properties and corresponding seasonal averages of climatic and hydrological factors at the basin scale, both for each individual river basin and for all five basins combined. To evaluate the relative influence of different factors on the spatial distribution of ZSD and FUI across the five major river basins, a generalized linear model (GLM) was applied (Dobson and Barnett, 2018). This multivariate regression approach incorporated environmental predictors—including annual mean climatic, hydrological, anthropogenic, watershed, and land cover variables—and allowed us to assess their respective contributions while accounting for potential multicollinearity among variables.

3. Results and discussion

3.1. Validation of Z_{SD} and FUI

To validate the accuracy of the satellite inversion of Z_{SD} and FUI, the *in-situ* data collected from specific locations were utilized. It was imperative that the timing of the data collection aligned closely with the satellite overpasses; hence, the *in-situ* measurements and the satellite imagery acquisition were required within a three-day window. Spatially, a 3 × 3 pixel window surrounding the location of each sampling point was extracted from the satellite image, and the mean value of these nine pixels was calculated. To ensure spatial consistency, the spatial coefficient of variation (CV), defined as the standard deviation divided by the mean of the nine pixels, needed to be less than 0.2 (Seegers et al., 2018).

To validate the feasibility of using a ± 3-day matching time window, we also conducted comparisons using a narrower ± 1-day window. As shown in Fig. 4, the Z_{SD} and FUI results obtained within the ± 1-day window are generally consistent with those from the ± 3-day window. However, the ± 3-day window significantly expands the matched dataset, allowing for more robust statistical comparisons. Therefore, the ± 3-day time window was ultimately adopted in this study. The Z_{SD} dataset used for model validation includes 60 pairs, with values ranging from 24.0 cm to 180.0 cm and an average of 88.0 cm; the FUI dataset comprised 46 pairs, with values from 6.0 to 19.0, averaging at 10.8 (Table 1).

The evaluation of Z_{SD} accuracy, as depicted in Fig. 4, revealed an R^2 of 0.78, an MAE of 15.4 cm, an MRE of 22.5 %, and a bias of −13.3 cm. The FUI results showed an R^2 of 0.86, an MAE of 1.54, an MRE of 19.9 %, and a bias of −1.07. The data analysis demonstrated that the line from the data points closely aligned with the match line, with nearly all points falling within the 95 % prediction area. This alignment demonstrates that Z_{SD} and FUI derived from Sentinel-2 MSI are largely consistent with *in-situ* measurements, confirming the effectiveness of the two satellite inversion methods.

3.2. Spatial distribution of Z_{SD} and FUI

Fig. 5 presents the longitudinal distributions of Z_{SD} and FUI along the main channels of the five rivers, based on multi-year (2019–2021) mean values, to illustrate the spatial patterns of river water optical properties. The Danube has the highest and stable Z_{SD} (avg. 96.0 cm; SD. 21.1 cm), while the Nile demonstrates broad variability (avg. 94.4 cm; SD. 62.8 cm). The Yangtze has moderate Z_{SD} (avg. 82.9 cm; SD. 50.3 cm), with some sections as low as 30 cm. The Mississippi has lower and stable Z_{SD} (avg. 62.5 cm; SD. 20.8 cm), and the Amazon has the lowest (avg. 35.4 cm; SD. 4.8 cm).

Table 1
Descriptive statistics of *in-situ* measurements for Z_{SD} and FUI.

Parameter	Sample size (N)	Min	Max	Mean	Median	Standard deviation
Z_{SD} (cm)	60	24.0	180.0	88.0	85.0	35.9
FUI	46	6.0	19.0	10.8	10.5	3.9

In Yangtze, a decrease in Z_{SD} is observed when moving from the upper to the middle and lower reaches ($p < 0.05$). Significant variations are noted in the upper reaches, particularly in segments between 4000–4500 km from the river mouth, where large dams have resulted in exceptionally high Z_{SD} values exceeding 200 cm; however, Z_{SD} decreases at tributary entrances. In Danube, Z_{SD} is high over 120 cm in the upper reaches but decreases as the river flows downstream, increasing again to over 100 cm near the Iron Gates Dam. In Mississippi, Z_{SD} decreases from the upper to the lower reaches ($p < 0.05$), with marked fluctuations in the upper and middle reaches influenced by numerous dams and tributaries. Z_{SD} stabilizes at approximately 40 cm in the lower reaches. Z_{SD} in the Nile generally rises from the upper to the lower reaches ($p < 0.05$), despite a decrease in the middle reaches after a peak before the Aswan High Dam. The Amazon Z_{SD} shows minimal variation, consistently

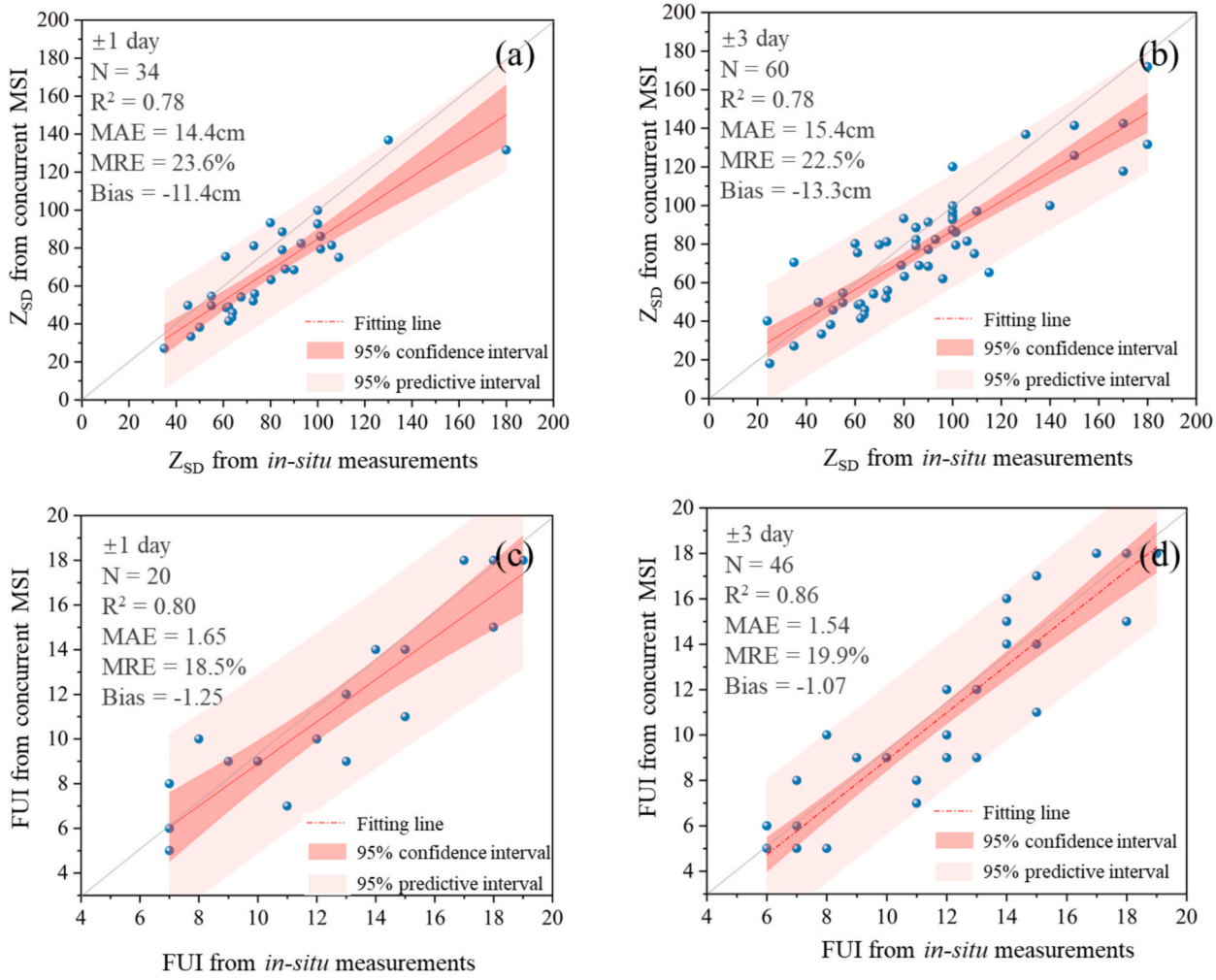

Fig. 4. Validation of Z_{SD} and FUI under ± 1-day and ± 3-day temporal matching windows. (a) Z_{SD} ± 1-day; (b) Z_{SD} ± 3-day; (c) FUI ± 1-day; (d) FUI ± 3-day.

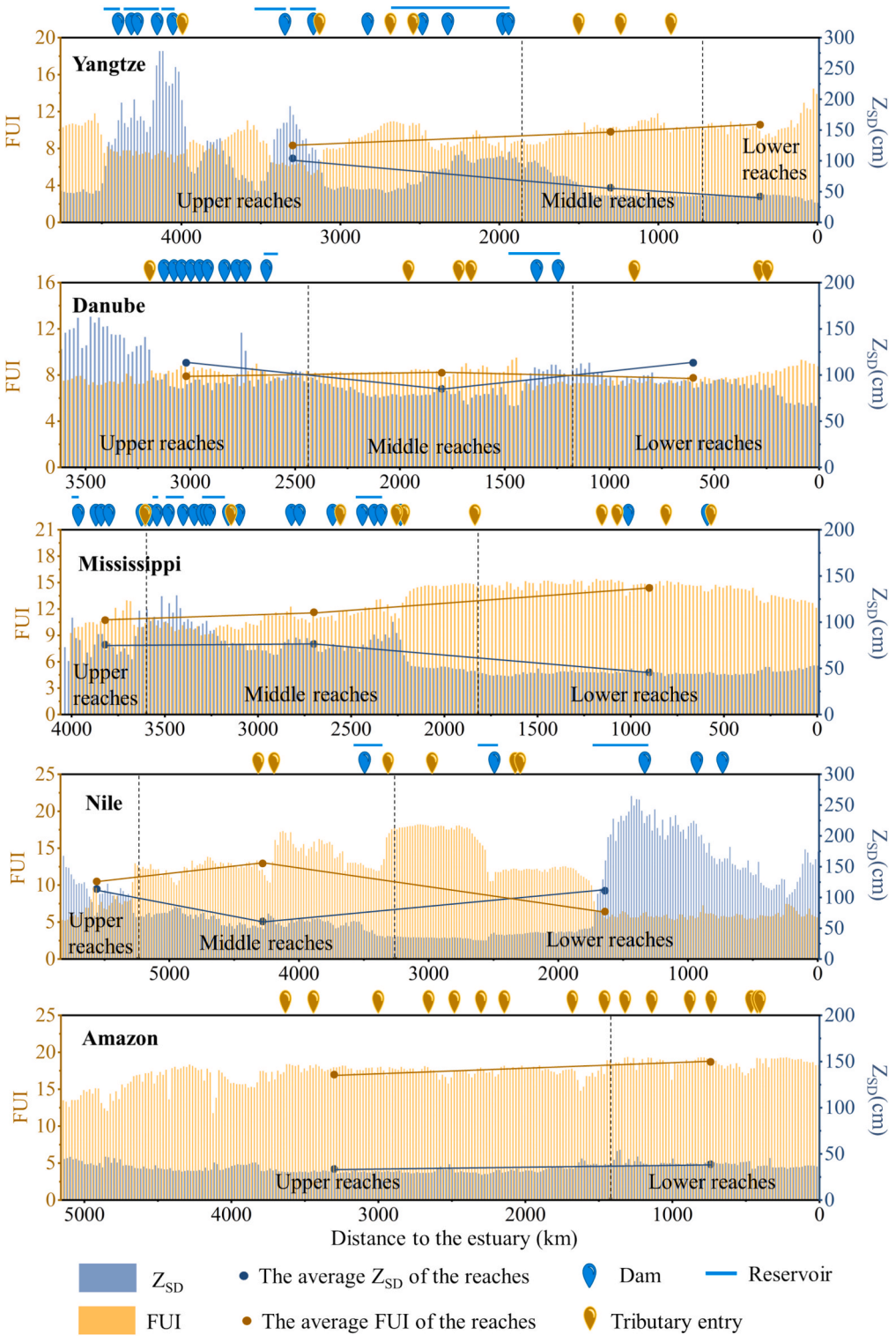

Fig. 5. Segmental mean Z_{SD} and FUI (2019–2021) along the main channels of the five rivers.

remaining around 30 cm. The general trend of FUI typically exhibits an inverse relationship with Z_{SD}, as lower FUI values generally suggest cleaner water. Fig. 5 shows the FUI levels of these rivers, supporting the idea that FUI and Z_{SD} are inversely related. This pattern is consistent with the distinct environmental characteristics of each river: for example, the Yangtze and Mississippi, both subject to high sediment loads and anthropogenic influences, show lower Z_{SD} and higher FUI values in downstream regions (Yang et al., 2004; Yin et al., 2023); the Nile's downstream clarity (higher Z_{SD} and lower FUI) is influenced by regulated flow and sediment trapping behind large dams (Elshemy and Meon, 2017); while the Amazon, characterized by year-round high temperatures and abundant rainfall, remains persistently turbid, with low Z_{SD} and high FUI values (Martinez et al., 2015).

Our results show that the water turbidity, ranging from clear to turbid, follows the sequence of Danube, Nile, Yangtze, Mississippi, and Amazon. While Yangtze, Mississippi, and Amazon exhibit increasing

turbidity from their upper to lower reaches, the lower reaches of Danube and Nile become less turbid downstream of the Iron Gates Dam and Aswan High Dam, respectively. This suggests the substantial influence of large dams on river water environments.

3.3. Seasonal variations of Z_{SD} and FUI

Fig. 6 illustrates Z_{SD} and FUI in the five rivers over spring, summer, autumn, and winter from 2019 to 2021. It points out areas where sharp changes in Z_{SD} and FUI occur and identifies the locations of dams, tributaries, and reservoirs. Fig. 7 presents statistical analyses of seasonal variations in Z_{SD} and FUI at the river basin scale.

The Mann-Whitney *U* test shows that most seasonal differences in the five rivers are significant ($p < 0.05$). However, the differences between spring and winter for Nile and Amazon and between summer and autumn for Mississippi are not significant. This study finds two opposite seasonal patterns in the five large rivers. In the first pattern, observed in tropical and subtropical rivers such as the Yangtze, Nile, and Amazon, water tends to be more turbid in summer and autumn but becomes clearer in spring and winter, with Z_{SD} increasing by 79.2 %, 15.4 %, and 33.7 %, respectively. In contrast, the other pattern is found in temperate systems like the Mississippi and Danube, where water is less clear in spring and winter but becomes clearer in summer and autumn. This trend is observed in the Mississippi and Danube, with Z_{SD} increasing by 24.4 % and 3.6 %, respectively. The seasonal variation patterns are generally consistent across different reaches of most rivers. However, exceptions exist, such as the Danube and Nile, where certain differences in seasonal trends are observed between different reaches. This may be attributed to the wide range of watersheds resulting in climatic variations between different reaches, and the influence of dam regulation and other factors.

Among the five rivers, Mississippi exhibits a distinct seasonal pattern compared to other rivers, with the maximum difference in average Z_{SD} between seasons reaching 31.4 %. The lowest Z_{SD} occurs in spring, with a mean of 53 cm, while the highest values are observed in Lake Pepin (117.5 cm). Notably, seasonal variations are particularly pronounced in the upper reaches, where Z_{SD} differences between spring and summer reach 59.4 cm. In contrast, Amazon has the lowest Z_{SD} and most stable changes across seasons, primarily driven by naturally high suspended sediment loads and dissolved organic matter from its extensive basin. Its Z_{SD} gradually decreases from upstream to downstream, which is probably related to the fact that no dams have been constructed along the main channel of Amazon, unlike other rivers.

Seasonal observations of FUI across the five rivers also reveal a clear inverse relationship with Z_{SD}, indicating they are strongly linked. For example, in Yangtze, Nile, and Amazon, higher FUI corresponds to lower Z_{SD} during summer and autumn, whereas lower FUI and higher Z_{SD} are observed in spring and winter (Fig. 7).

3.4. The driving factors of the spatial and seasonal pattern

3.4.1. Impact of water conservancy infrastructure on the spatial abruptions of Z_{SD} and FUI

Our results showed that abrupt spatial changes in Z_{SD} of the five

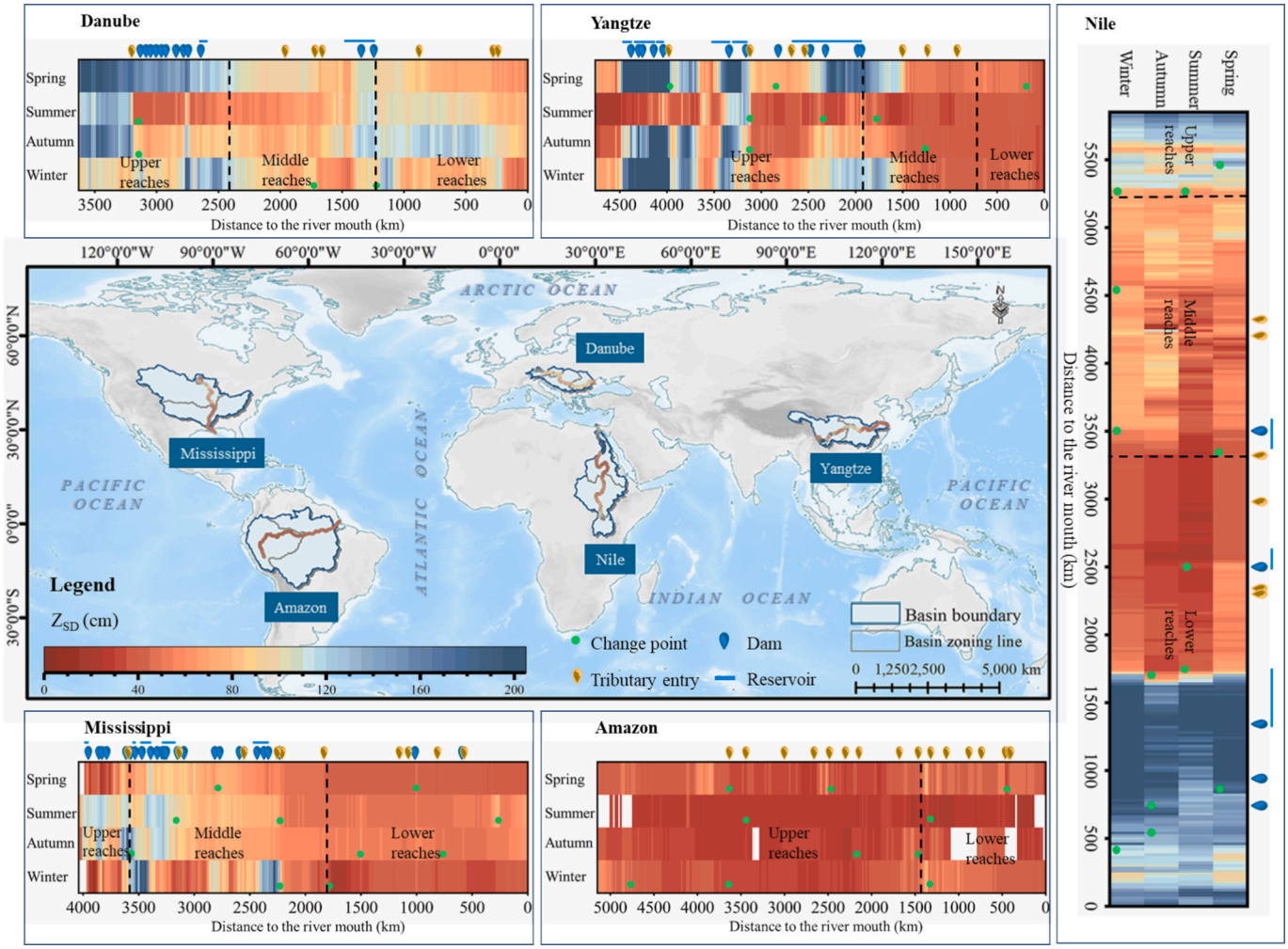

Fig. 6. Longitudinal distributions of Z_{SD} and FUI in the five rivers across spring, summer, autumn, and winter.

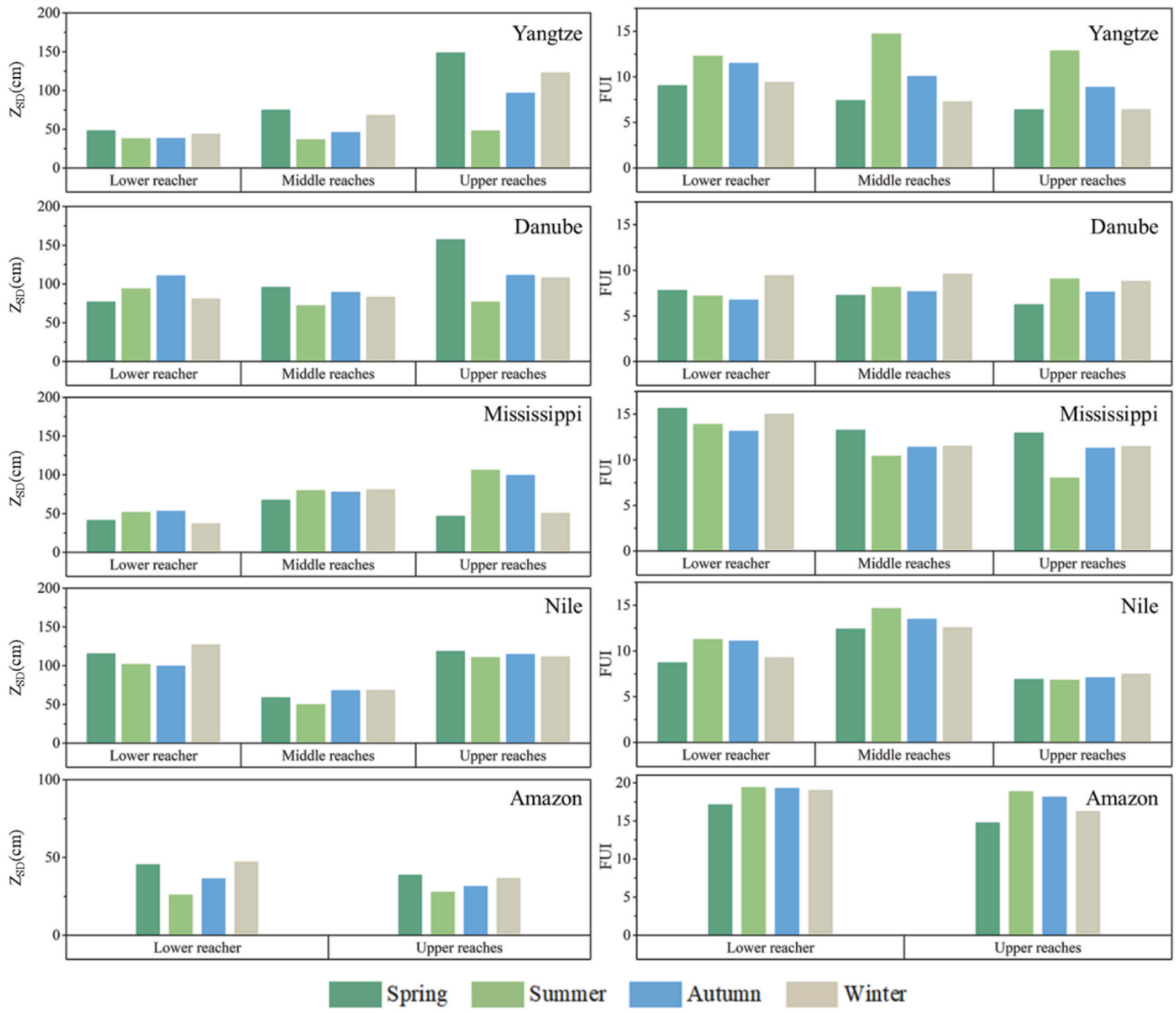

Fig. 7. Seasonal variation of Z_{SD} and FUI in the five river basins.

rivers are predominantly associated with anthropogenic activities and tributary confluences (Fig. 6). It was found that 37.8 % of the sharp change points in water quality are situated within approximately 20 km of the dams or reservoirs constructed along the river, indicating a strong statistical association between water conservancy infrastructure and spatial variation of river water properties. Dams primarily function by trapping sediment and storing water, which reduces the quantity of suspended solids flowing downstream, thereby influencing the spatial variation in river water quality (Sun et al., 2025). For example, due to the construction of the Iron Gates and Aswan Dams, the water in the lower reaches of Danube and Nile is clearer compared to their upper and middle reaches. Conversely, Amazon has significantly fewer dams compared to other rivers, reflecting a lower level of human intervention and correspondingly murkier waters.

Tributary confluences also show a notable association with sharp changes in water quality, with 42.2 % of sharp change points identified within 20 km of these sites. The sediment and dissolved organic matter content in tributaries often differ from the main channel, potentially introducing either higher or lower concentrations of suspended solids and nutrients (Qiu et al., 2024). Our statistical analysis showed that 79 % of sharp change points near tributaries were associated with decreased Z_{SD}, while 21 % showed increased Z_{SD}. For instance, after the Min River, a tributary of Yangtze, merges with the main channel, Z_{SD} decreases by 42.4 %, and FUI increases by 38.9 %. Similarly, when the Missouri River merges with Mississippi, Z_{SD} decreases by 29.2 % while FUI rises by 22.5 % (Fig. 6). Note that some change points are associated with both dams and tributaries, and approximately 31.1 % of the sharp change points are located outside these two categories.

3.4.2. *Impact of basin environment and climate factors on Z_{SD} and FUI across the five rivers*

River water quality is influenced by the combined impacts of climate change, land cover, and hydraulic infrastructure (Hou et al., 2024). These factors affect the spatial and seasonal variations in Z_{SD} and FUI. To further understand the primary driving factors of spatial heterogeneity in Z_{SD} and FUI, GLM was used to analyze how different environmental factors contribute to these variations (Fig. 8).

The GLM analysis of spatial variation in Z_{SD} across the five rivers identifies K and PRE as the most pertinent factors (Fig. 8b). The K indicates the susceptibility of soil to erosion by water. In scenarios with

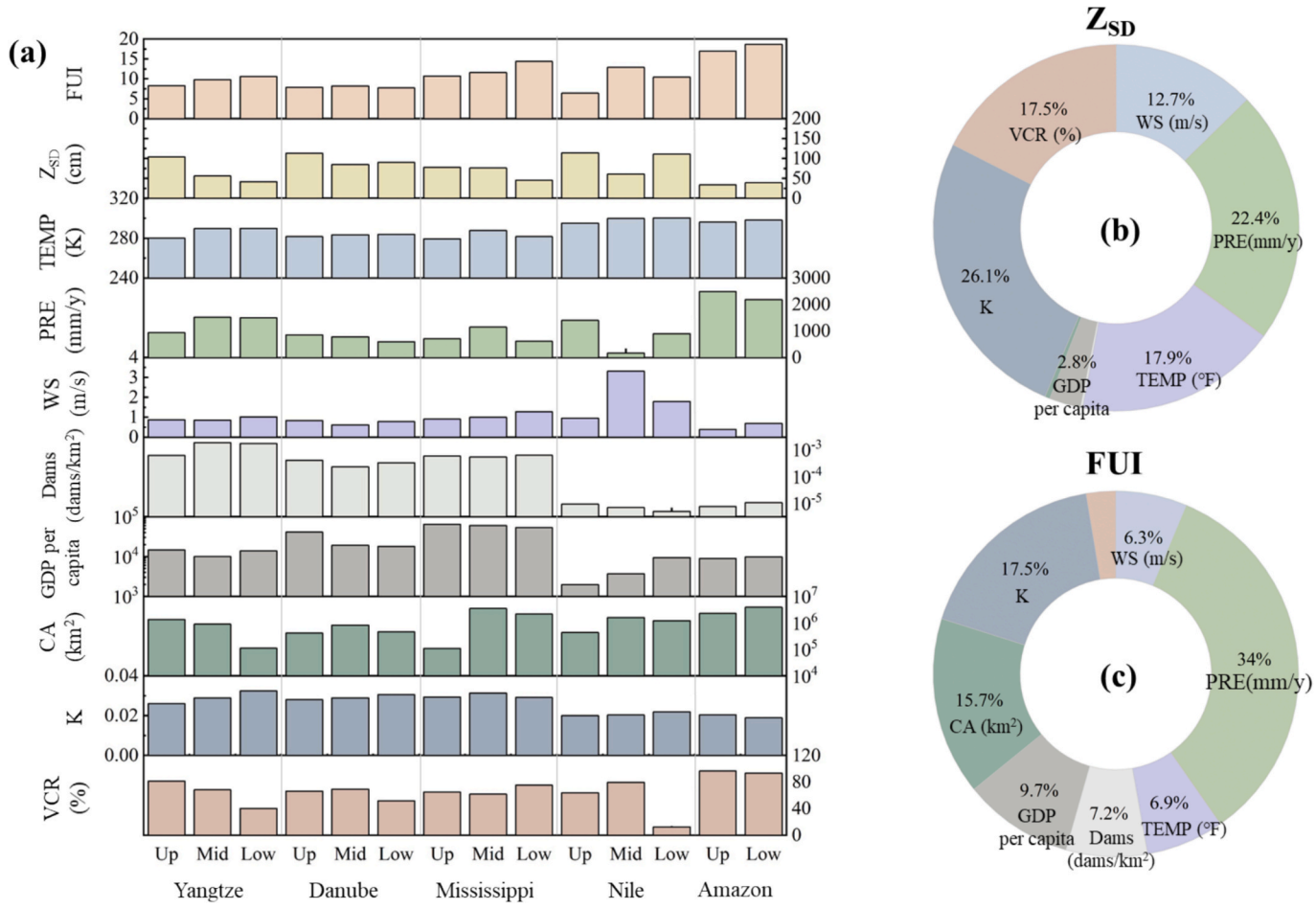

Fig. 8. (a) Statistical distribution of annual mean Z_{SD} and FUI across the five rivers, along annual mean temperature (TEMP), annual mean precipitation (PRE), annual mean wind speed (WS), Dam density, Gross domestic product (GDP) per capita, catchment area (CA), Soil erodibility factor (K), and vegetation coverage rate (VCR). (b) and (c) Contributions of various factors to the spatial distribution of Z_{SD} and FUI in the five rivers.

similar rainfall, soils with higher K are more prone to erosion compared to those less susceptible (Cassol et al., 2018). For example, despite comparable precipitation levels in the spring and autumn seasons in the upper reaches of Mississippi and Yangtze, higher K in the upper Mississippi may account for its lower Z_{SD}. That is because eroded soil may increase the sediment load in the river, thus reducing Z_{SD} (Piqué et al., 2014). On the other hand, PRE may influence the amount of runoff, which can carry soil into rivers and increase water turbidity (Wu et al., 2014). In this study, the Amazon, with an extraordinary annual rainfall exceeding 2000 mm in its basin, has the lowest Z_{SD} of the five rivers. Moreover, the decomposition of vast plant debris in rainforests further adds to the organic matter, exacerbating water turbidity (Neill et al., 2001; Shah et al., 2022). In addition, spatial variations in ZSD are also affected by TEMP (17.9 %), VCR (17.5 %), and WS (12.7 %). Higher temperatures can promote organic matter decomposition, increasing water turbidity (Xiang et al., 2019). Greater vegetation coverage helps reduce soil erosion, thereby improving transparency (Qiu et al., 2024). Higher wind speeds may resuspend bottom sediments, leading to lower transparency (Zhang et al., 2023a).

The GLM analysis of spatial variation in FUI also identifies PRE and K as the primary factors influencing FUI, corroborating findings from Z_{SD} analysis (Fig. 8c). It is noticeable that PRE exerts a greater impact on FUI than K, but K has a more significant impact on Z_{SD} than PRE. This is likely due to that PRE not only significantly increases the TSM in rivers through surface runoff but also introduces more organic matter (Tornevi et al., 2014), while K may predominantly affect the suspended solids in rivers.

3.4.3. *Impact of the basin climatic factors on the seasonal variations of river Z_{SD} and FUI*

The findings presented in section 3.3 reveal variations in the seasonal patterns of Z_{SD} and FUI among different river basins. To delve deeper into the factors driving these seasonal changes, we conducted a correlation analysis between Z_{SD}, FUI, and seasonal meteorological and hydrological factors such as WS, PRE, TEMP, and WL within each basin. This analysis aims to examine how these factors influence the seasonal distribution of water optical properties, as detailed in Table 2.

At the scale of all five rivers, Z_{SD} and FUI showed stronger correlations with PRE (Z_{SD}: $r = -0.73$; FUI: $r = 0.69$) and WL (Z_{SD}: $r = -0.84$; FUI: $r = 0.88$) than with TEMP or WS. Specifically, PRE generally shows negative correlations with Z_{SD} and positively correlated with FUI. This may indicate that rainfall enhances surface runoff, transporting sediment and nutrients into the river, thereby increasing turbidity and altering water color (Wu et al., 2014). This effect of PRE is particularly evident in the upstream reaches. For example, the correlation coefficients between PRE and Z_{SD} of the upper Yangtze, Nile, and Amazon are -0.87, -0.95, and -0.85, respectively. These strong responses may be attributed to the higher elevations, where river flow is primarily driven by regional rainfall with relatively fewer human disturbances, allowing water quality to respond more directly to PRE (Abd-El Monsef et al., 2015). Similarly, WL also exhibits a predominantly positive correlation with FUI and a negative correlation with Z_{SD}, reinforcing the critical role of hydrological processes in material transport within rivers. When WL rises, it often means more runoff, which brings in more sediment and organic matter (Syvitski et al., 2005). This relationship is

Table 2
Pearson correlation between Z_{SD}, FUI, and meteorological and hydrological factors for the five rivers.

River	Reach	Parameter	WS (m/s)	PRE (mm)	TEMP (K)	WL (m)
Yangtze	Upper	Z_{SD}	0.73	−0.87	−0.71	−0.9
	reaches	FUI	−0.88	0.96	0.86	0.91
	Middle	Z_{SD}	−0.39	−0.41	−0.73	−0.27
	reaches	FUI	0.03	0.71	0.87	0.58
	Lower	Z_{SD}	−0.66	−0.43	−0.52	−0.88
	reaches	FUI	0.47	0.65	0.77	0.9
Danube	Upper	Z_{SD}	0.44	−0.67	−0.49	−0.1
	reaches	FUI	−0.04	0.43	0.15	0.16
	Middle	Z_{SD}	0.75	−0.75	−0.53	−0.65
	reaches	FUI	−0.04	0.05	−0.28	0.08
	Lower	Z_{SD}	−0.61	−0.23	0.39	−0.93
	reaches	FUI	0.99	−0.27	−0.78	0.45
Mississippi	Upper	Z_{SD}	0.44	0.86	0.77	−0.74
	reaches	FUI	0.02	−0.76	−0.68	0.65
	Middle	Z_{SD}	0.32	−0.66	−0.02	−0.96
	reaches	FUI	0.26	0.98	0.27	0.88
	Lower	Z_{SD}	−0.22	0.56	0.81	−0.61
	reaches	FUI	−0.3	−0.08	−0.47	0.92
Nile	Upper	Z_{SD}	0.42	−0.95	0.34	0.23
	reaches	FUI	−0.72	0.33	0.54	−0.08
	Middle	Z_{SD}	0.71	−0.83	−0.77	−0.17
	reaches	FUI	−0.8	0.99	0.74	0.64
	Lower	Z_{SD}	0.92	−0.83	0.43	0.88
	reaches	FUI	−0.57	0.79	−0.85	−0.82
Amazon	Upper	Z_{SD}	−0.67	−0.85	0.19	−0.4
	reaches	FUI	0.5	0.77	−0.38	0.58
	Lower	Z_{SD}	−0.22	−0.93	0.42	−0.22
	reaches	FUI	0.5	0.46	−0.97	0.82
Five rivers		Z_{SD}	0.23	−0.73	−0.65	−0.84
		FUI	−0.25	0.69	0.64	0.88

more pronounced in the middle and lower reaches, where WL is more sensitive to cumulative upstream inputs and is often influenced by reservoir operations and tributary inflows. For instance, in the lower Yangtze, Danube, and Nile, the correlation coefficients between Z_{SD} and WL are −0.88, −0.93, and 0.88, respectively. These patterns may be attributed to the regulation effects of major dams such as the Three Gorges Dam, Iron Gate Dam, and Aswan High Dam (Nistor et al., 2021; Yang et al., 2018).

At the basin scale, the seasonal variation patterns of Z_{SD} and FUI in the five rivers are predominantly influenced by the climate type and flood season in each river basin. The Yangtze, Nile, and Amazon are all mainly situated in subtropical/tropical zones—they experience concentrated precipitation during summer-autumn flood seasons (Hassan, 1981; Yu et al., 2009). This seasonal rainfall results in a significant decrease in Z_{SD} and an elevation of FUI compared to spring and winter. Among the five rivers, the Danube and Mississippi are located in higher-latitude regions and are more affected by complex climate types (Bisselink et al., 2018). The Danube lies between temperate oceanic, temperate continental, and Mediterranean climates. Both temperate continental and subtropical monsoon climates influence Mississippi. Due to these mixed climate types, their flood seasons are influenced by both rainfall and snowmelt in spring and winter. These seasonal changes can be seen in the patterns of Z_{SD} and FUI.

3.5. Similarities and differences in the observed Z_{SD} and FUI

Z_{SD} and FUI are essential optical properties of water bodies, and both have long been used as key parameters for assessing water quality. Z_{SD} is influenced by the attenuation of light underwater, which depends on the concentrations of dissolved and suspended substances, affecting both light absorption and scattering. Theoretically, Z_{SD} is mainly determined by the minimum value of K_d (Lee et al., 2015). Similarly, like Z_{SD}, FUI is also influenced by the concentrations of various substances in the water, which in turn affect the water's color. By utilizing the hue angle α as a continuous counterpart to FUI, satellite data from any available hue angle algorithm can be employed to estimate FUI (Van der Woerd and Wernand, 2018). Notably, both FUI and Z_{SD} remote sensing models are relatively straightforward and exhibit strong global applicability, making them well-suited for large-scale remote sensing monitoring studies.

Previous studies have established the correlation between Z_{SD} and FUI in both inland and marine water. Brewin et al. (2023) found a close inverse relationship between FUI and Z_{SD}, with FUI explaining 73–83 % of the variation in Z_{SD}. However, some distinctions exist between these two parameters. For example, Pitarch et al. (2021) analyzed FUI and Z_{SD} trends in the North Atlantic, revealing that in regions with small trends, Z_{SD} and FUI exhibited opposing trends. The study highlighted that these two parameters do not entirely capture the same information, suggesting that further research is necessary. Additionally, Pitarch et al. (2019) observed that when FUI values were low, Z_{SD} displayed a broader range of variation, potentially linked to the unique characteristics of different marine regions. This suggests that low FUI values are not reliable parameters of oligotrophic oceans. Conversely, when FUI values were high, the variation in Z_{SD} diminished, and when FUI exceeded 17, Z_{SD} tended to stabilize. This could be attributed to the water in these regions reaching a highly turbid state, where further changes in light attenuation no longer significantly affect Z_{SD}.

In this study, in addition to identifying a significant negative correlation between FUI and Z_{SD} ($r = -0.76$), we also observed that when Z_{SD} reaches relatively low levels (e.g., $Z_{SD} < 50$ cm), the corresponding distribution of FUI is notably broad (Fig. 9). This may be attributed to the stronger light absorption and scattering in highly turbid waters. Under such conditions, changes in Z_{SD} may not effectively reflect further variations in water quality, thereby limiting its ability to differentiate between distinct water states. In contrast, FUI remains effective in distinguishing these states. Additionally, when Z_{SD} is relatively high, the trend of decreasing FUI with increasing Z_{SD} becomes less noticeable (e.g., FUI < 7). This finding aligns with Pitarch et al. (2021), who observed that color changes at the bluer end of the spectrum are less perceptible to the human eye. In such cases, Z_{SD} continues to be an effective parameter of water states. These observations suggest that the sensitivity of Z_{SD} and FUI differs in highly turbid and clear inland waters, with their changes not always perfectly aligned. Consequently, these two parameters can complement each other, and it is crucial to monitor both Z_{SD} and FUI in water quality assessments.

3.6. Implications for SDG 6.3.2 evaluation in rivers

SDG 6.3.2 focuses on the proportion of good surface water quality, but there is a serious lack of data on river water quality globally due to the difficulty in obtaining river water quality parameters through traditional sampling methods (Water, 2016). As Z_{SD} serves as a core parameter for water management agencies worldwide (Kaika, 2003), studies have taken Z_{SD} as the proxy of water quality and demonstrated the utility of satellite-derived Z_{SD} in SDG 6.3.2 assessment for lakes and reservoirs (Qiu et al., 2023; Shen et al., 2020). Here we applied the satellite-derived Z_{SD} and FUI to the SDG 6.3.2 assessment for rivers and obtained the first reporting of SDG 6.3.2 in large rivers across the world. The 10th percentile (30.4 cm) of seasonal Z_{SD} from the five rivers was taken as the compliance threshold, following a previous study (Shen et al., 2020). For each river segment, if Z_{SD} met the standard in more than 75 % of seasons, its water quality was classified as "good" during the monitoring period.

Fig. 10 illustrates the water quality classification of the five rivers based on Z_{SD}, revealing that 72 % of the analyzed river segments meet "good" water quality. The proportion of good water quality in the Amazon main channel is lowest, with only 14.7 %. As discussed in Section 3.4, high rainfall and dense vegetation in the Amazon basin cause surface erosion and plant litter decomposition. This increases TSM and CDOM in the river, worsening water turbidity (Valerio et al., 2024). In contrast, the Danube has 100 % good water quality. This is likely due

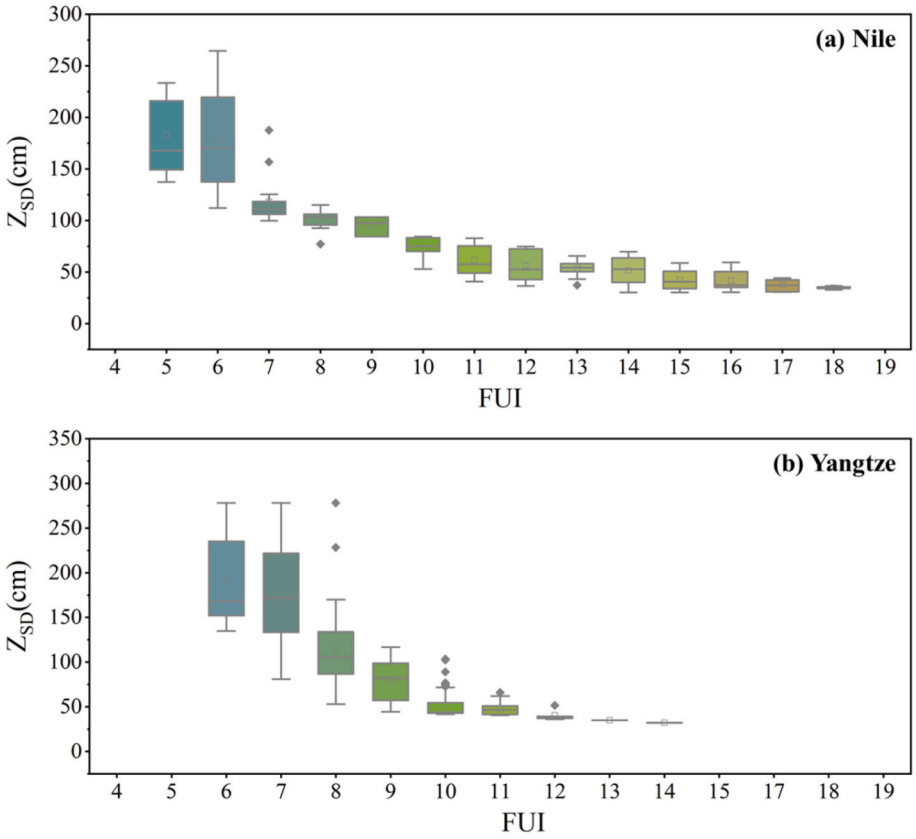

Fig. 9. Box plot of Z_{SD} and FUI observed in the Nile and Yangtze.

to effective hydraulic infrastructure regulation and low soil erodibility in the Danube basin (Nistor et al., 2021). Moderate rainfall also reduces surface erosion and sediment transport, keeping the water clear. For the main channels of the other rivers, the proportion of good water quality is 92.1 % in the Mississippi, 87.4 % in the Yangtze, and 78.5 % in the Nile. Following the same threshold determination method as Z_{SD}, FUI less than 17.4 was defined as the threshold for "good" water quality. The results of the two standards were generally consistent, with an overall relative difference of 9.8 % in the five rivers. The establishment of remote sensing methodologies for river Z_{SD} and FUI, particularly their application in SDG 6.3.2 assessments, enables satellite-based, globally consistent water quality monitoring in rivers. Although these satellite-based methods were not able to directly detect non-optical pollutants (e.g., nitrogen/phosphorus/heavy metals) in water, they provide rapid screening capabilities and can serve as a valuable complement to conventional monitoring, thereby significantly enhancing the coverage and comparability of global river water quality datasets. In addition, it should be noted that seasonal averaged monitoring and assessment may potentially mask certain critical short-term fluctuations in river dynamics. Therefore, this highlights the critical need for satellite observations with both high spatial and temporal resolution to adequately characterize river system dynamics.

4. Conclusions

This study presents a comprehensive assessment of turbidity dynamics in five major river systems across continents through the lens of optical water quality parameters. The key findings and implications can be summarized as follows:

(1) Spatial heterogeneity analysis reveals a distinct transparency gradient among the studied rivers, with Danube exhibiting the highest transparency (mean $Z_{SD} = 0.96$ m), followed by Nile (mean $Z_{SD} = 0.94$ m), Yangtze (mean $Z_{SD} = 0.83$ m), Mississippi (mean $Z_{SD} = 0.63$ m), and Amazon (mean $Z_{SD} = 0.35$ m). Basin-specific characteristics, particularly soil erodibility (K-factor) and precipitation patterns (PRE), were found to account for approximately 50 % of the observed inter-river variability.

(2) Anthropogenic and geomorphological controls were quantitatively identified, with 37.8 % of abrupt Z_{SD} transitions occurring within 20 km of major dams (e.g., Iron Gates, Aswan Dams) and reservoirs, and 42.2 % concentrated at tributary entries. These findings underscore the profound impacts of hydrological engineering on river optical properties.

(3) Seasonal dynamics exhibit two distinct patterns strongly correlated with basin hydrology. Tropical and subtropical rivers (Amazon, Nile, and Yangtze) show maximum turbidity during peak discharge seasons (summer-autumn), while temperate systems (Danube and Mississippi) display different patterns due to snowmelt and rainfall regimes. Moreover, the analyses show that precipitation (PRE) generally has high correlations to seasonal Z_{SD} variance in upper reaches, which decrease in sediment-rich lower reaches.

(4) The complementary nature of Z_{SD} and FUI is quantitatively demonstrated through their differential sensitivity across turbidity gradients. While strongly inversely correlated ($r = -0.79$), FUI shows greater discriminative capacity in highly turbid conditions ($Z_{SD} < 0.5$ m), whereas Z_{SD} provides better resolution in clearer waters (FUI < 7).

(5) SDG 6.3.2 assessment reveals 72 % of analyzed river segments meet "good" water quality standards, with the Amazon showing the lowest proportion of "good" water quality segments (14.7 %). This baseline evaluation highlights critical gaps in achieving SDG6.3.2 targets in rivers.

These findings advance our understanding of large-scale river optical properties through several novel contributions: (i) establishment of the first global benchmark for river transparency and color metrics, (ii) analysis of anthropogenic and climatic drivers of the spatial–temporal variations in river water optical properties, and (iii) suggesting the

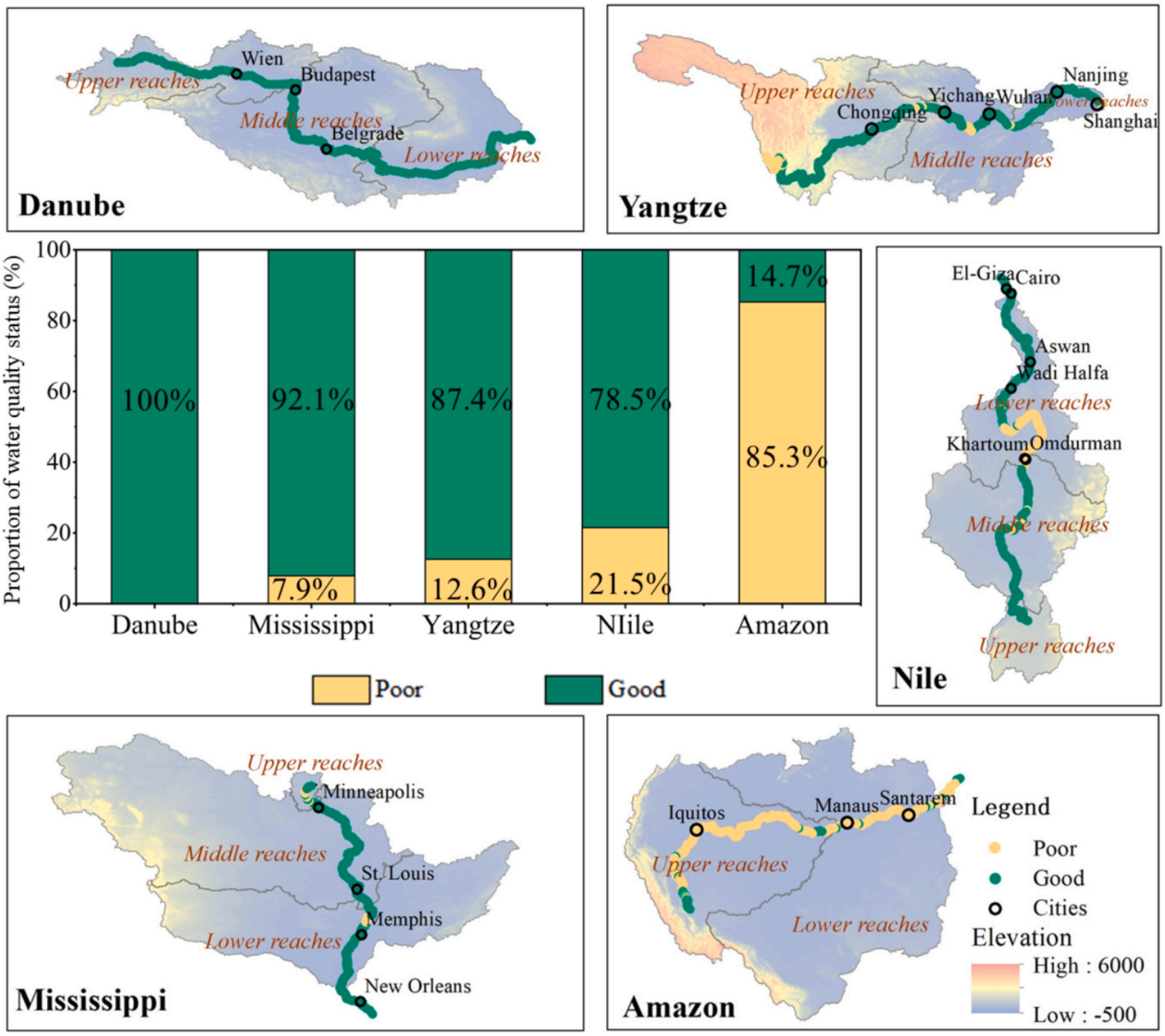

Fig. 10. SDG 6.3.2 assessment results for the five rivers.

satellite-based method for SDG 6.3.2 reporting in rivers. By integrating a systematic methodological framework with comprehensive analysis, this study provides valuable insights for policymakers to implement targeted water quality interventions and track progress toward SDG 6 targets.

CRediT authorship contribution statement

Xuezhu Jiang: Writing – original draft, Visualization, Software, Methodology, Formal analysis, Data curation. **Shenglei Wang:** Writing – review & editing, Supervision, Project administration, Methodology, Conceptualization. **Junsheng Li:** Resources, Funding acquisition, Formal analysis. **Evangelos Spyrakos:** Writing – review & editing, Methodology. **Huaxin Yao:** Visualization, Software. **Fangfang Zhang:** Methodology. **Andrew N. Tyler:** Writing – review & editing, Investigation. **Bing Zhang:** Writing – review & editing, Project administration.

Declaration of competing interest

The authors declare that they have no known competing financial interests or personal relationships that could have appeared to influence the work reported in this paper.

Acknowledgement

We would like to thank Professor Yunmei Li from Nanjing Normal University for providing the *in situ* data in Yangtze River, and the European Space Agency for providing the Sentinel-2 MSI data. The field work in the Danube Delta part of AMC PhD work, jointly funded by GeoEcoMar and the University of Stirling. This research has been jointly sponsored by the National Key Research and Development Program of China (Grant No. 2022YFC3800701), the International Partnership Program of Chinese Academy of Sciences (Grant No. 313GJHZ2022085FN), the Scientific and Disruptive Technology Research Fund Project of Aerospace Information Research Institute, Chinese Academy of Sciences (Grant No. 2025-AIRCAS-SDTP-16), and the Future Star Program of Aerospace Information Research Institute Chinese Academy of Sciences.

Appendix A. Supplementary data

Supplementary data to this article can be found online at https://doi.org/10.1016/j.jag.2025.104826.

Data availability

Data will be made available on request.

References

Abd-El Monsef, H., Smith, S.E., Darwish, K., 2015. Impacts of the Aswan High Dam after 50 years. Water Resour. Manag. 29, 1873–1885.

Ali, A., Zhou, G., Lopez, F.P.A., Xu, C., Jing, G., Tan, Y., 2024. Deep learning for water quality multivariate assessment in inland water across China. Int. J. Appl. Earth Obs. Geoinf. 133, 104078.

Bisselink, B., de Roo, A., Bernhard, J., Gelati, E., 2018. Future projections of water scarcity in the Danube River Basin due to land use, water demand and climate change. Journal of Environmental Geography 11, 25–36.

Brewin, R.J., Pitarch, J., Dall'Olmo, G., van der Woerd, H.J., Lin, J., Sun, X., Tilstone, G. H., 2023. Evaluating historic and modern optical techniques for monitoring phytoplankton biomass in the Atlantic Ocean. Frontiers in Marine Science 10, 1111416.

Camberlin, P., 2009. Nile basin climates, the Nile: origin, environments, limnology and human use. Springer 307–333.

Cao, Z., Shen, M., Kutser, T., Liu, M., Qi, T., Ma, J., Ma, R., Duan, H., 2022. What water color parameters could be mapped using MODIS land reflectance products: a global evaluation over coastal and inland waters. Earth Sci. Rev. 232, 104154.

Cassol, E.A., Silva, T.S.d., Eltz, F.L.F., Levien, R., 2018. Soil erodibility under natural rainfall conditions as the K factor of the universal soil loss equation and application of the nomograph for a subtropical Ultisol. Revista Brasileira de Ciência do Solo 42, e0170262.

Ceola, S., Laio, F., Montanari, A., 2019. Global-scale human pressure evolution imprints on sustainability of river systems. Hydrol. Earth Syst. Sci. 23, 3933–3944.

Chadwick, A., Steel, E., Williams-Schaetzel, R., Passalacqua, P., Paola, C., 2022. Channel migration in experimental river networks mapped by particle image velocimetry. J. Geophys. Res. Earth 127, e2021JF006300.

Corbane, C., Politis, P., Kempeneers, P., Simonetti, D., Soille, P., Burger, A., Pesaresi, M., Sabo, F., Syrris, V., Kemper, T., 2020. A global cloud free pixel-based image composite from Sentinel-2 data. Data Brief 31, 105737.

Dobson, A.J., Barnett, A.G., 2018. An introduction to generalized linear models. Chapman and Hall/CRC.

Doxsey-Whitfield, E., MacManus, K., Adamo, S.B., Pistolesi, L., Squires, J., Borkovska, O., Baptista, S.R., 2015. Taking advantage of the improved availability of census data: a first look at the gridded population of the world, version 4. Pap. Appl. Geogr. 1, 226–234.

Drusch, M., Del Bello, U., Carlier, S., Colin, O., Fernandez, V., Gascon, F., Hoersch, B., Isola, C., Laberinti, P., Martimort, P., 2012. Sentinel-2: ESA's optical high-resolution mission for GMES operational services. Remote Sens. Environ. 120, 25–36.

Duan, H., Cao, Z., Luo, J., Shen, M., 2025. AI-driven opportunities and challenges in lake remote sensing. Information. Geography 100014.

Elshemy, M., Meon, G., 2017. Water Quality Assessment of Aswan High Dam Reservoir. In: Negm, A.M. (Ed.), The Nile River. Springer International Publishing, Cham, pp. 105–143.

Fabricius, K., Logan, M., Weeks, S., Lewis, S., Brodie, J., 2016. Changes in water clarity in response to river discharges on the Great Barrier Reef continental shelf: 2002–2013. Estuar. Coast. Shelf Sci. 173, A1–A15.

Gardner, J.R., Yang, X., Topp, S.N., Ross, M.R., Altenau, E.H., Pavelsky, T.M., 2021. The color of rivers. Geophys. Res. Lett. 48, e2020GL088946.

Gasparotti, C.M., 2014. The main factors of water pollution in Danube River basin. Euro Economica 33, 91–106.

González-Estrada, E., Villaseñor, J.A., Acosta-Pech, R., 2022. Shapiro-Wilk test for multivariate skew-normality. Comput. Stat. 37, 1985–2001.

Hassan, F.A., 1981. Historical Nile floods and their implications for climatic change. Science 212, 1142–1145.

He, Y., Lu, Z., Wang, W., Zhang, D., Zhang, Y., Qin, B., Shi, K., Yang, X., 2022. Water clarity mapping of global lakes using a novel hybrid deep-learning-based recurrent model with Landsat OLI images. Water Res. 215, 118241.

Hou, X., Xie, D., Feng, L., Shen, F., Nienhuis, J.H., 2024. Sustained increase in suspended sediments near global river deltas over the past two decades. Nat. Commun. 15, 3319.

Huang, J., Zhang, Y., Bing, H., Peng, J., Dong, F., Gao, J., Arhonditsis, G.B., 2021. Characterizing the river water quality in China: recent progress and on-going challenges. Water Res. 201, 117309.

Jiang, D., Matsushita, B., Setiawan, F., Vundo, A., 2019. An improved algorithm for estimating the Secchi disk depth from remote sensing data based on the new underwater visibility theory. ISPRS J. Photogramm. Remote Sens. 152, 13–23.

Kaika, M., 2003. The Water Framework Directive: a new directive for a changing social, political and economic European framework. Eur. Plan. Stud. 11, 299–316.

Kuhn, C., Valerio, A., Ward, N., Loken, L., Sawakuchi, H., Kampel, M., Richey, J., Stadler, P., Crawford, J., Striegl, R., Vermote, E., Pahlevan, N., Butman, D., 2019. Performance of Landsat-8 and Sentinel-2 surface reflectance products for river remote sensing retrievals of chlorophyll-a and turbidity. Remote Sens. Environ. 224, 104–118.

Lee, Z., Arnone, R., Boyce, D., Franz, B., Greb, S., Hu, C., Lavender, S., Lewis, M., Schaeffer, B., Shang, S., 2018a. Global water clarity: continuing a century-long monitoring. Eos 99.

Lee, Z., Shang, S., Du, K., Wei, J., 2018b. Resolving the long-standing puzzles about the observed Secchi depth relationships. Limnol. Oceanogr. 63, 2321–2336.

Lee, Z., Shang, S., Hu, C., Du, K., Weidemann, A., Hou, W., Lin, J., Lin, G., 2015. Secchi disk depth: a new theory and mechanistic model for underwater visibility. Remote Sens. Environ. 169, 139–149.

Lehmann, M.K., Gurlin, D., Pahlevan, N., Alikas, K., Conroy, T., Anstee, J., Balasubramanian, S.V., Barbosa, C.C.F., Binding, C., Bracher, A., Bresciani, M., Burtner, A., Cao, Z., Dekker, A.G., Di Vittorio, C., Drayson, N., Errera, R.M., Fernandez, V., Ficek, D., Fichot, C.G., Gege, P., Giardino, C., Gitelson, A.A., Greb, S. R., Henderson, H., Higa, H., Rahaghi, A.I., Jamet, C., Jiang, D., Jordan, T., Kangro, K., Kravitz, J.A., Kristoffersen, A.S., Kudela, R., Li, L., Ligi, M., Loisel, H., Lohrenz, S., Ma, R., Maciel, D.A., Malthus, T.J., Matsushita, B., Matthews, M., Minaudo, C., Mishra, D.R., Mishra, S., Moore, T., Moses, W.J., Nguyễn, H., Novo, E. M.L.M., Novoa, S., Odermatt, D., O'Donnell, D.M., Olmanson, L.G., Ondrusek, M., Oppelt, N., Ouillon, S., Pereira Filho, W., Plattner, S., Verdú, A.R., Salem, S.I., Schalles, J.F., Simis, S.G.H., Siswanto, E., Smith, B., Somlai-Schweiger, I., Soppa, M. A., Spyrakos, E., Tessin, E., van der Woerd, H.J., Vander Woude, A., Vandermeulen, R.A., Vantrepotte, V., Wernand, M.R., Werther, M., Young, K., Yue, L., 2023. GLORIA - a globally representative hyperspectral in situ dataset for optical sensing of water quality. Sci. Data 10, 100.

Lehner, B., Grill, G., 2013. Global river hydrography and network routing: baseline data and new approaches to study the world's large river systems. Hydrol. Process. 27, 2171–2186.

Li, L., Knapp, J.L., Lintern, A., Ng, G.-H.-C., Perdrial, J., Sullivan, P.L., Zhi, W., 2024. River water quality shaped by land–river connectivity in a changing climate. Nat. Clim. Chang. 14, 225–237.

Liang, Y.-C., Lo, M.-H., Lan, C.-W., Seo, H., Ummenhofer, C.C., Yeager, S., Wu, R.-J., Steffen, J.D., 2020. Amplified seasonal cycle in hydroclimate over the Amazon river basin and its plume region. Nat. Commun. 11, 4390.

Liu, X., Lee, Z., Zhang, Y., Lin, J., Shi, K., Zhou, Y., Qin, B., Sun, Z., 2019. Remote sensing of secchi depth in highly turbid lake waters and its application with MERIS data. Remote Sens. (Basel) 11, 2226.

Louis, J., Debaecker, V., Pflug, B., Main-Knorn, M., Bieniarz, J., Mueller-Wilm, U., Cadau, E., Gascon, F., 2016. Sentinel-2 Sen2Cor: L2A processor for users, Proceedings of the Living Planet Symposium, Prague, Czech Republic, pp. 9-13.

Luo, J., Duan, H., Xu, Y., Shen, M., Zhang, Y., Xiao, Q., Ni, G., Wang, K., Xin, Y., Qi, T., Feng, L., Qiu, Y., Jeppesen, E., Woolway, R.I., 2025. Global trends and regime state shifts of lacustrine aquatic vegetation. The Innovation 6.

Maciel, D.A., Pahlevan, N., Barbosa, C.C., Martins, V.S., Smith, B., O'Shea, R.E., Balasubramanian, S.V., Saranathan, A.M., Novo, E.M., 2023. Towards global long-term water transparency products from the Landsat archive. Remote Sens. Environ. 299, 113889.

Main-Knorn, M., Pflug, B., Louis, J., Debaecker, V., Müller-Wilm, U., Gascon, F., 2017. Sen2Cor for Sentinel-2, Proc.SPIE, p. 1042704.

Mann, H.B., 1945. Nonparametric tests against trend. Econometrica 245–259.

Martinez, J.M., Espinoza-Villar, R., Armijos, E., Silva Moreira, L., 2015. The optical properties of river and floodplain waters in the Amazon River Basin: Implications for satellite-based measurements of suspended particulate matter. J. Geophys. Res. Earth 120, 1274–1287.

Narayanan, A., Cohen, S., Gardner, J.R., 2024. Riverine sediment response to deforestation in the Amazon basin. Earth Surf. Dyn. 12, 581–599.

Neill, C., Deegan, L.A., Thomas, S.M., Cerri, C.C., 2001. Deforestation for pasture alters nitrogen and phosphorus in small amazonian streams. Ecol. Appl. 11, 1817–1828.

Nistor, C., Săvulescu, I., Mihai, B.-A., Zaharia, L., Vîrghileanu, M., Carablaisă, S., 2021. The impact of large dams on fluvial sedimentation: the Iron Gates Reservoir on the Danube River. Acta Geogr. Slov. 61, 41–55-41–55.

Otsu, N., 1979. A Threshold selection Method from Gray-Level Histograms. Systems, Man and Cybernetics, IEEE Transactions on 9, 62–66.

Pekel, J.-F., Cottam, A., Gorelick, N., Belward, A.S., 2016. High-resolution mapping of global surface water and its long-term changes. Nature 540, 418–422.

Piqué, G., López-Tarazón, J.A., Batalla, R.J., 2014. Variability of in-channel sediment storage in a river draining highly erodible areas (the Isábena, Ebro Basin). J. Soil. Sediment. 14, 2031–2044.

Pitarch, J., Bellacicco, M., Marullo, S., Van Der Woerd, H.J., 2021. Global maps of Forel–Ule index, hue angle and Secchi disk depth derived from 21 years of monthly ESA Ocean Colour climate Change Initiative data. Earth Syst. Sci. Data 13, 481–490.

Pitarch, J., van der Woerd, H.J., Brewin, R.J., Zielinski, O., 2019. Optical properties of Forel-Ule water types deduced from 15 years of global satellite ocean color observations. Remote Sens. Environ. 231, 111249.

Qiu, R., Wang, S., Shi, J., Shen, W., Zhang, W., Zhang, F., Li, J., 2023. Sentinel-2 MSI Observations of Water Clarity in Inland Waters across Hainan Island and Implications for SDG 6.3.2 Evaluation. Remote Sens. (Basel) 15, 1600.

Qiu, Z., Liu, D., Duan, M., Chen, P., Yang, C., Li, K., Duan, H., 2024. Four-decades of sediment transport variations in the Yellow River on the Loess Plateau using Landsat imagery. Remote Sens. Environ. 306, 114147.

Seegers, B.N., Stumpf, R.P., Schaeffer, B.A., Loftin, K.A., Werdell, P.J., 2018. Performance metrics for the assessment of satellite data products: an ocean color case study. Opt. Express 26, 7404–7422.

Shah, N.W., Baillie, B.R., Bishop, K., Ferraz, S., Högbom, L., Nettles, J., 2022. The effects of forest management on water quality. For. Ecol. Manage. 522, 120397.

Shen, M., Duan, H., Cao, Z., Xue, K., Qi, T., Ma, J., Liu, D., Song, K., Huang, C., Song, X., 2020. Sentinel-3 OLCI observations of water clarity in large lakes in eastern China: Implications for SDG 6.3. 2 evaluation. Remote Sens. Environ. 247, 111950.

Sommerwerk, N., Bloesch, J., Paunović, M., Baumgartner, C., Venohr, M., Schneider-Jacoby, M., Hein, T., Tockner, K., 2010. Managing the world's most international river: the Danube River Basin. Mar. Freshw. Res. 61, 736–748.

Song, K., Wang, Q., Liu, G., Jacinthe, P.-A., Li, S., Tao, H., Du, Y., Wen, Z., Wang, X., Guo, W., 2022. A unified model for high resolution mapping of global lake (> 1 ha) clarity using Landsat imagery data. Sci. Total Environ. 810, 151188.
Sun, X., Tian, L., Fang, H., Walling, D.E., Huang, L., Park, E., Li, D., Zheng, C., Feng, L., 2025. Changes in global fluvial sediment concentrations and fluxes between 1985 and 2020. Nat. Sustainability 1–10.
Syvitski, J.P., Vörösmarty, C.J., Kettner, A.J., Green, P., 2005. Impact of humans on the flux of terrestrial sediment to the global coastal ocean. Science 308, 376–380.
Toming, K., Kutser, T., Laas, A., Sepp, M., Paavel, B., Nõges, T., 2016. First experiences in mapping lake water quality parameters with Sentinel-2 MSI imagery. Remote Sens. (Basel) 8, 640.
Tornevi, A., Bergstedt, O., Forsberg, B., 2014. Precipitation effects on microbial pollution in a river: lag structures and seasonal effect modification. PLoS One 9, e98546.
Valerio, A.M., Kampel, M., Vantrepotte, V., Ballester, V., Richey, J., 2024. Assessment of Atmospheric Correction Algorithms for Sentinel-3 OLCI in the Amazon River Continuum. Remote Sens. (Basel) 16 (380), 371–382.
Van der Woerd, H.J., Wernand, M.R., 2015. True colour classification of natural waters with medium-spectral resolution satellites: SeaWiFS, MODIS, MERIS and OLCI. Sensors 15, 25663–25680.
Van der Woerd, H.J., Wernand, M.R., 2018. Hue-angle product for low to medium spatial resolution optical satellite sensors. Remote Sens. (Basel) 10, 180.
Van Vliet, M.T., Thorslund, J., Strokal, M., Hofstra, N., Flörke, M., Ehalt Macedo, H., Nkwasa, A., Tang, T., Kaushal, S.S., Kumar, R., 2023. Global river water quality under climate change and hydroclimatic extremes. Nature Reviews Earth & Environment 4, 687–702.
Vörösmarty, C.J., McIntyre, P.B., Gessner, M.O., Dudgeon, D., Prusevich, A., Green, P., Glidden, S., Bunn, S.E., Sullivan, C.A., Liermann, C.R., 2010. Global threats to human water security and river biodiversity. Nature 467, 555–561.
Wang, J., Walter, B., Yao, F., Song, C., Ding, M., Maroof, A., Zhu, J., Fan, C., McAlister, J., Sikder, S., 2022. GeoDAR: georeferenced global dams and reservoirs dataset for bridging attributes and geolocations. Earth Syst. Sci. Data 14, 1869–1899.
Wang, S., Jiang, X., Spyrakos, E., Li, J., McGlinchey, C., Constantinescu, A.M., Tyler, A. N., 2024. Water color from Sentinel-2 MSI data for monitoring large rivers: Yangtze and Danube. Geo-spatial Inf. Sci. 27, 854–869.
Wang, S., Lee, Z., Shang, S., Li, J., Zhang, B., Lin, G., 2019. Deriving inherent optical properties from classical water color measurements: Forel-Ule index and Secchi disk depth. Opt. Express 27, 7642–7655.
Wang, S., Li, J., Zhang, B., Shen, Q., Zhang, F., Lu, Z., 2016. A simple correction method for the MODIS surface reflectance product over typical inland waters in China. Int. J. Remote Sens. 37, 6076–6096.
Wang, S., Li, J., Zhang, B., Spyrakos, E., Tyler, A.N., Shen, Q., Zhang, F., Kuster, T., Lehmann, M.K., Wu, Y., Peng, D., 2018. Trophic state assessment of global inland waters using a MODIS-derived Forel-Ule index. Remote Sens. Environ. 217, 444–460.
Wang, S., Li, J., Zhang, W., Cao, C., Zhang, F., Shen, Q., Zhang, X., Zhang, B., 2021. A dataset of remote-sensed Forel-Ule Index for global inland waters during 2000–2018. Sci. Data 8, 26.
Wen, Z., Wang, Q., Ma, Y., Jacinthe, P.A., Liu, G., Li, S., Shang, Y., Tao, H., Fang, C., Lyu, L., 2024. Remote estimates of suspended particulate matter in global lakes using machine learning models. International Soil and Water Conservation Research 12, 200–216.
Werther, M., Odermatt, D., Simis, S.G., Gurlin, D., Lehmann, M.K., Kutser, T., Gupana, R., Varley, A., Hunter, P.D., Tyler, A.N., 2022. A Bayesian approach for remote sensing of chlorophyll-a and associated retrieval uncertainty in oligotrophic and mesotrophic lakes. Remote Sens. Environ. 283, 113295.
Wu, J., Qian, H., Li, P., Song, Y., 2014. A system-theory-based model for monthly river runoff forecasting: model calibration and optimization. Journal of Hydrology and Hydromechanics 62, 82–88.
Wu, Q., Ke, L., Wang, J., Pavelsky, T.M., Allen, G.H., Sheng, Y., Duan, X., Zhu, Y., Wu, J., Wang, L., Liu, K., Chen, T., Zhang, W., Fan, C., Yong, B., Song, C., 2023. Satellites reveal hotspots of global river extent change. Nat. Commun. 14, 1587.
Xiang, H., Zhang, Y., Atkinson, D., Sekar, R., 2019. Combined effects of water temperature, grazing snails and terrestrial herbivores on leaf decomposition in urban streams. PeerJ 7, e7580.
Yan, D., Wang, K., Qin, T., Weng, B., Wang, H., Bi, W., Li, X., Li, M., Lv, Z., Liu, F., 2019. A data set of global river networks and corresponding water resources zones divisions. Sci. Data 6, 219.
Yang, H., Yang, S., Xu, K., Milliman, J., Wang, H., Yang, Z., Chen, Z., Zhang, C., 2018. Human impacts on sediment in the Yangtze River: a review and new perspectives. Global Planet. Change 162, 8–17.
Yang, S., Shi, Z., Zhao, H., Li, P., Dai, S., Gao, A., 2004. Research note: Effects of human activities on the Yangtze River suspended sediment flux into the estuary in the last century. Hydrol. Earth Syst. Sci. 8, 1210–1216.
Yang, X., Pavelsky, T.M., Allen, G.H., Donchyts, G., 2020. RivWidthCloud: an Automated Google Earth Engine Algorithm for River Width Extraction from Remotely Sensed Imagery. IEEE Geosci. Remote Sens. Lett. 17, 217–221.
Ye, M., Sun, Y., 2022. Review of the Forel–Ule Index based on in situ and remote sensing methods and application in water quality assessment. Environ. Sci. Pollut. Res. 29, 13024–13041.
Yeşilköy, S., Baydaroğlu, Ö., Demir, I., 2024. Is snow drought a messenger for the upcoming severe drought period? a case study in the upper Mississippi river basin. Atmos. Res. 309, 107553.
Yin, S., Gao, G., Li, Y., Xu, Y.J., Turner, R.E., Ran, L., Wang, X., Fu, B., 2023. Long-term trends of streamflow, sediment load and nutrient fluxes from the Mississippi River Basin: Impacts of climate change and human activities. J. Hydrol. 616, 128822.
Yu, F., Chen, Z., Ren, X., Yang, G., 2009. Analysis of historical floods on the Yangtze River, China: Characteristics and explanations. Geomorphology 113, 210–216.
Yue, L., Zhang, L., Peng, R., Zeng, C., Duan, H., Shen, H., 2024. Understanding the potential, Uncertainties, and Limitations of Spatiotemporal Fusion for monitoring Chlorophyll a Concentration in Inland Eutrophic Lakes. Journal of Remote Sensing 4, 0209.
Zhang, B., Guo, J., Rong, Z., Lv, X., 2023a. Variations of remote-sensed Forel-Ule Index in the Bohai and Yellow seas during 1997–2019. Remote Sens. (Basel) 15, 3487.
Zhang, X., Dong, Z., Gupta, H., Wu, G., Li, D., 2016. Impact of the three Gorges Dam on the hydrology and ecology of the Yangtze River. Water 8, 590.
Zhang, Y., He, X., Lian, G., Bai, Y., Yang, Y., Gong, F., Wang, D., Zhang, Z., Li, T., Jin, X., 2023b. Monitoring and spatial traceability of river water quality using Sentinel-2 satellite images. Sci. Total Environ. 894, 164862.